

Textural, thermal, and topographic constraints on lava flow system structure: the December 2010 eruption of Piton de la Fournaise

Arianna Soldati, Andrew J.L. J.L. Harris, Lucia Gurioli, Nicolas Villeneuve, M. Rhéty, F. Gomez, A. Whittington

▶ **To cite this version:**

Arianna Soldati, Andrew J.L. J.L. Harris, Lucia Gurioli, Nicolas Villeneuve, M. Rhéty, et al.. Textural, thermal, and topographic constraints on lava flow system structure: the December 2010 eruption of Piton de la Fournaise. Bulletin of Volcanology, 2018, 80 (10), 10.1007/s00445-018-1246-9 . hal-01877248

HAL Id: hal-01877248
https://uca.hal.science/hal-01877248

Submitted on 7 Nov 2018

HAL is a multi-disciplinary open access archive for the deposit and dissemination of scientific research documents, whether they are published or not. The documents may come from teaching and research institutions in France or abroad, or from public or private research centers.

L'archive ouverte pluridisciplinaire **HAL**, est destinée au dépôt et à la diffusion de documents scientifiques de niveau recherche, publiés ou non, émanant des établissements d'enseignement et de recherche français ou étrangers, des laboratoires publics ou privés.

Textural, thermal, and topographic constraints on lava flow system structure: the December 2010 eruption of Piton de la Fournaise

A. Soldati[1] · A. J. L. Harris[2] · L. Gurioli[2] · N. Villeneuve[3,4] · M. Rhéty[2] · F. Gomez[1] · A. Whittington[1]

Abstract

In this study, we examine the channel-fed ʻaʻā lava flow system that was emplaced during a very short (less than 15 h long) eruption at Piton de la Fournaise (La Réunion) in December 2010. The system had four branches, the longest of which was 1100 m long. Three branches were emplaced over a smooth-surfaced pāhoehoe flow field with a vertical relief of 1–2 m and did not undergo burial by subsequent events. The fourth branch erupted from the same vent as the 1957 eruption and re-used the pre-existing channels of that eruption. In the proximal–medial sections of the three systems that were unconfined, we identified channelized flow sections that were characterized by the presence of either a single channel or multiple braided channels. These fed short (30–260 m long) zones of dispersed flow in the distal sections. We subsequently investigated the role of lava rheology (as controlled by downflow variations in crystal and bubble content) and pre-existing topography in triggering the transitions between single-channel and braided channel flow sections. Crystal content was 10 to 70 vol% and vesicle content was 18 to 55 vol%; cooling rates over distance (derived from glass chemistry) were 11 °C/km to 27 °C/km. However, downflow textural and thermal evolution appeared to neither affect, nor be affected by, whether the channel was single or braided. Instead, the channel network architecture could be related to even modest underlying slope variations. Here, a slope increase resulted in channel confluence, and a slope decrease resulted in channel bifurcation. This process was reversible, in that downflow slope variation could drive the channel network architecture to switch back and forth between a single channel and multiple braided channels several times along its length. Dispersed flow is always present immediately behind the flow front, irrespective of underlying topography. Three previous studies of basaltic lava flows found that steeper slopes favored braided channels, the opposite of what was observed here. We suggest that the underlying substrate and lava type may exert a control on this behavior, but further studies remain necessary.

Introduction

The architecture of a channel-fed lava flow system was classically described by Lipman and Banks (1987). At the flow-system scale, Lipman and Banks (1987) recognized four zones down a channel-fed lava flow: (i) a stable channel zone; (ii) a transitional channel zone, bounded by incipient rubble levées; (iii) a dispersed flow zone; and (iv) the flow front. This flow architecture has been recognized at several volcanic systems on Earth, ranging in composition from basaltic (Kilburn and Guest 1993) to silicic (Harris et al. 2004), as well as on other terrestrial planets such as Mars (Garry et al. 2007). We define the channel as a zone of flowing lava contained between static levées (e.g., Sparks et al. 1976; Lipman and Banks 1987; Kilburn and Guest 1993), which typically begins to form quite close behind the dispersed flow zone (Rhéty et

Electronic supplementary material The online version of this article (https://doi.org/10.1007/s00445 018 1246 9) contains supplementary material, which is available to authorized users.

✉ A. Soldati
arianna.soldati@mizzou.edu

[1] Department of Geological Sciences, University of Missouri, Columbia, MO 65211 1380, USA

[2] CNRS, IRD, OPGC, Laboratoire Magmas et Volcans, Université Clermont Auvergne, F 63000 Clermont Ferrand, France

[3] Observatoire Volcanologique du Piton de la Fournaise, Institut de Physique du Globe de Paris, Sorbonne Paris Cité, CNRS, Université Paris Diderot, F 75005 Paris, France

[4] Laboratoire GéoSciences Réunion, Institut de Physique du Globe de Paris, Sorbonne Paris Cité, CNRS, Université de La Réunion, F 97744 Saint Denis, France

al. 2017). Following the definition of Lipman and Banks (1987), the dispersed flow zone is an unstructured zone where there are no levées present, and the flow core is covered in breccia all the way to the flow front. Rubble levées are laid down by the initial flow front passage (Sparks et al. 1976) and may later become overprinted with overflow levées (e.g., Lipman and Banks 1987; Naranjo et al. 1992; Bailey et al. 2006). Overflow levées are emplaced during periods of increased effusion rate, when flux exceeds channel capacity, causing the channel to overflow for a short period of time (Bailey et al. 2006). During waning flow, levées become accreted to the inner walls of the channel (Naranjo et al. 1992), and nested levées may form (Lipman and Banks 1987).

Pre-existing topography has been shown to affect the form of the channel network (single channel versus braided channel) down such lava flow systems. Dietterich and Cashman (2014) studied the effect of slope on channel networks at Mauna Loa, finding that steeper slopes corresponded to higher braiding indices. Here, following Dietterich and Cashman (2014), we assess the effect of slope on the spatial variation of channel network architecture by comparing ground slope changes and observed channel network structure. Additionally, we examine the potential interactions of textural parameters with the flow structure by quantifying downflow cooling, crystallinity, and porosity and analyzing them in the context of the observed flow system architecture. We focus on the channelized flow system emplaced by the December 2010 eruption of Piton de la Fournaise (La Réunion, France). This system was emplaced during an extremely short-lived eruption, resulting in the simplest possible flow field, which minimized the number of emplacement variables to be considered. We find that the relation between slope and flow system architecture previously found in other systems (Krauskopf 1948; Dietterich and Cashman 2014), and at the same volcano (Rhéty et al. 2017), cannot be applied globally.

Piton de la Fournaise: the December 2010 eruption and lava flow field

Piton de la Fournaise is located on the Island of La Réunion, in the Indian Ocean. The most common present-day eruptive activity at Piton de la Fournaise consists of short-duration eruptions, lasting between one day and a few months (Bachèlery et al. 2016). These eruptions generally occur within the Enclos Fouqué (Fig. 1), i.e., the most recent caldera of the volcano (Villeneuve and Bachèlery 2006). Activity is typically effusive, and erupted volumes are generally low, with dense rock equivalent volumes of less than 10^7 m^3 per eruption (Roult et al. 2012; Bachèlery et al. 2016). Mean output rates (MOR) are generally 1–10 m^3/s with peak time-averaged discharge rates (TADR) of up to 60 m^3/s (Coppola et al. 2017). We define MOR as the total erupted volume divided by the total duration of the eruption, TADR as the volume erupted during a known time window within the eruptive period, and effusion rate as an instantaneous flux (Harris et al. 2007, 2017). Most effusive events at Piton de la Fournaise are characterized by TADR that decay rapidly with time and are coupled with syn-eruptive deflation of the summit (Coppola et al. 2017). This means that, during an eruption, TADRs and effusion rates begin at a level higher than the MOR and then decay, in an exponential fashion, through it (Harris et al. 2000, 2007). As argued by Coppola et al. (2017), this pattern is consistent with rapid withdrawal of magma from a pressurized source (Wadge 1981).

The December 2010 eruption was a typical Piton de la Fournaise short-duration, low-volume, effusive eruption occurring within the Enclos Fouqué (Fig. 1). Enhanced seismicity was first reported between 07:48 and 08:01 (hh:mm, all times are local, UTC+4) on December 9 (Di Muro 2010a), and a second phase of enhanced seismicity was recorded between 08:35 and 09:53 on the same day (Di Muro 2010b). Both events were associated with summit inflation and a threefold increase in SO_2 emission (Di Muro 2010c). A third phase of enhanced seismicity and summit inflation began at 19:08 (Di Muro 2010d). The eruption began at the end of this seismic crisis around 22:40 from a location on the NNW flank of the volcano (Di Muro 2010e). Lava flows were reported as descending the north-west flank of Piton de La Fournaise at 06:45 on the following morning (Di Muro 2010f), but the eruption was declared over at 14:50, with no seismic activity having been recorded since 13:30 (Di Muro 2010g). The eruption thus lasted less than 15 h.

We chose this channel system as the focus of our study for four main reasons. First, the flow field is easily accessible and its areal extent is limited, allowing high spatial-resolution mapping and sampling. Second, the flow morphological features (main and secondary channels, multiple generations of levées, overflows, lava morphologies) are fresh and well-exposed, facilitating their identification. Third, because the eruption was of short duration, few channel sections were buried by later flow. Fourth, and most importantly, the flow consists of four different branches fed by the same magma over a short period of time, allowing us to focus solely on the effects of pre-existing topography and downflow cooling and crystallization on channel system architecture. Google Earth-based mapping by Rhéty (2014) identified four en-échelon fissure segments associated with the December 2010 eruption. These were orientated SSE–NNW and extended over a distance of 225 m from an elevation of 2515 m a.s.l. down to 2450 m a.s.l. The fissure segments fed four channelized ‘a‘ā flows, named south, west, north-west, and north, which extended to a distance of up to 1.2 km from the eruptive fissure (Rhéty 2014). The total flow area was previously estimated as being 0.269 km^2 which, given a typical flow thickness of 2 m, gives a flow field volume of 0.54×10^6 m^3 for a MOR of 9.8 m^3/s (Harris et al. 2016).

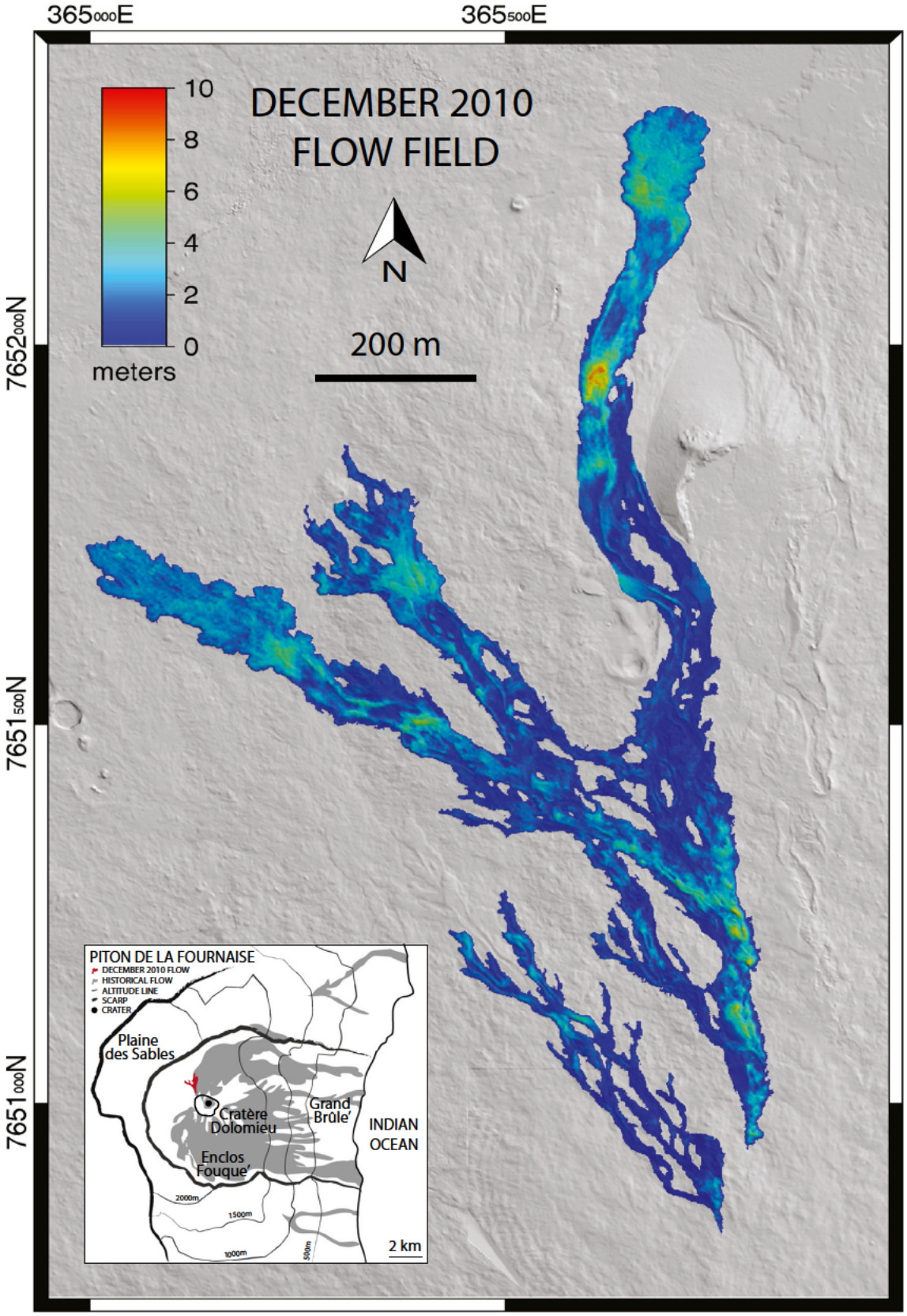


Fig. 1 DEM of the December 2010 flow field area, highlighting flow thickness. Coordinates are in meters (UTM 40S). Inset: Piton de la Fournaise map showing the location of the December 2010 flow

Methods

Mapping

A preliminary map of the December 2010 lava flow field was produced on the basis of satellite images provided by Google Earth©. Specifically, toggling between the pre-eruption image of December 4, 2010 (Image © 2018 Digital Globe) and the post-eruption image of February 16, 2012 (Image © 2018 Digital Globe) allowed us to delimit the flows emitted during the December 2010 eruption. The pre-eruptive images were also used to map and define pre-existing flows underlying and/or adjacent to the 2010 flow units, such as the 1957 and 2000 channel-fed ʻaʻā flow fields.

This preliminary map was later refined on the basis of two digital elevation models (DEMs) of the study area. The first, pre-eruptive, DEM was produced in 2010 by the Institut Géographique National (IGN) from an airborne Light Detection and Ranging (LIDAR) dataset. That DEM was used to extract pre-existing terrain slope downflow. The second, post-eruptive DEM was produced in 2018 photogrammetrically using 209 images acquired with a Canon 5DSR camera (51 MegaPixel resolution) with a 50-mm lens mounted on a ultra-light aircraft. From this photogrammetric DEM, cross-flow profiles were extracted every 10 m along the middle of each flow branch, allowing us to determine flow and channel width (Supplementary Material Table 1). The photogrammetric DEM was constructed in Agisoft Photoscan Pro. The two DEMs were downsampled to a horizontal resolution of 1 m and co-aligned using an affine transformation to minimize differences in spatial orientation (RMS error of 0.45 m for areas excluding the lava flow). The difference between the post-eruptive and pre-eruptive DEMs, calculated using ArcGIS, allowed us to precisely determine the flow thickness and volume.

Mapping was supported by analysis of thermal (7.5–13 μm) images collected during the morning of December 10 using a hand-held thermal camera (Fig. 2). During a site visit by the personnel of the Observatoire de Physique du Globe (Di Muro 2010g), 38 thermal images were acquired from Pas de Bellecombe, a location on the caldera rim 2.5 km west of the eruptive fissure, between 05:25 and 06:00. Images were collected with a hand-held FLIR Systems ThermaCam PM695 operating in the low gain (-40–120 °C) range. Image size was 320 × 240 pixels with 1.3 mrad pixels, which over a distance of 2.5 km gives a pixel size of 3.25 m. Images were oblique, but provided an overview of the flow field allowing dimensions and relative surface temperatures of each flow to be analyzed.

Field-based measurements and sampling

Channel dimension measurements and sampling were conducted during three field visits in 2013, 2014, and 2016. All measurements and sampling sites were GPS-located. For each flow, the master channel was followed and the depth and width of the channel was measured with tape measure and compass-clinometer, as were the height and width of the levées. The depth of undrained lava in the channel was obtained by subtracting levée inner and outer height (see, for example, Fig. 11 of Favalli et al. (2018) for definition of the measured and derived channel/levée geometries). Where braided, the dimensions of each channel making up the total width of the channel system were measured, and the morphology of the channel lava and levée type (initial, nested, accretionary, or overflow) were noted. A total of 23 scaled morphological profiles were completed.

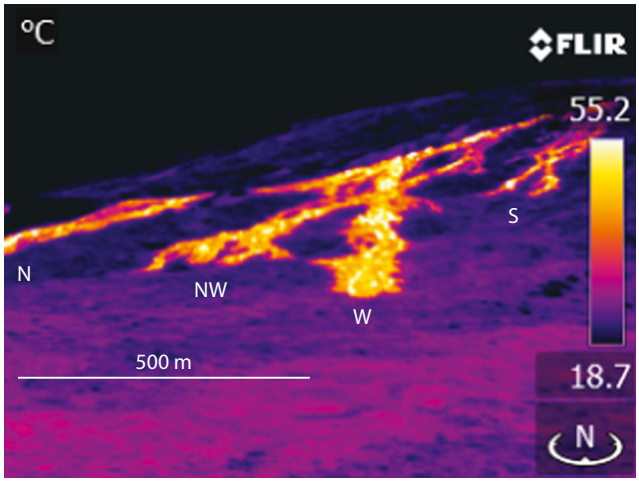


Fig. 2 Thermal imagery of the December 2010 flow field

A total of 55 samples were collected (Fig. 3). The west flow was sampled in detail, with one sample being collected every ~ 30 m down channel between the vent and the flow front. The other three flows were sampled focusing on the vent (i.e., the source), the flow front, and around slope breaks, resulting in the collection of six-to-nine samples per flow. Samples were collected in situ and consisted mostly of core extrusions and accretionary levées where glass was visible (Table 1).

Estimation of volume fluxes

Flow areas and volumes were estimated from the flow map. The MOR was obtained by dividing the flow volume by the eruption duration, and effusion rates in master channels were estimated using field-based measurements of the channel dimensions. To do this, first, we calculated mean flow velocity in the channel using Jeffreys' equation (Jeffreys 1925) with an estimated lava viscosity of 380 Pa s (Harris et al. 2015) and a bulk density of 1080 kg/m^3. Multiplying the velocity by flow cross-sectional area (flow width × depth) provided an estimate of the peak effusion rate under bankfull conditions.

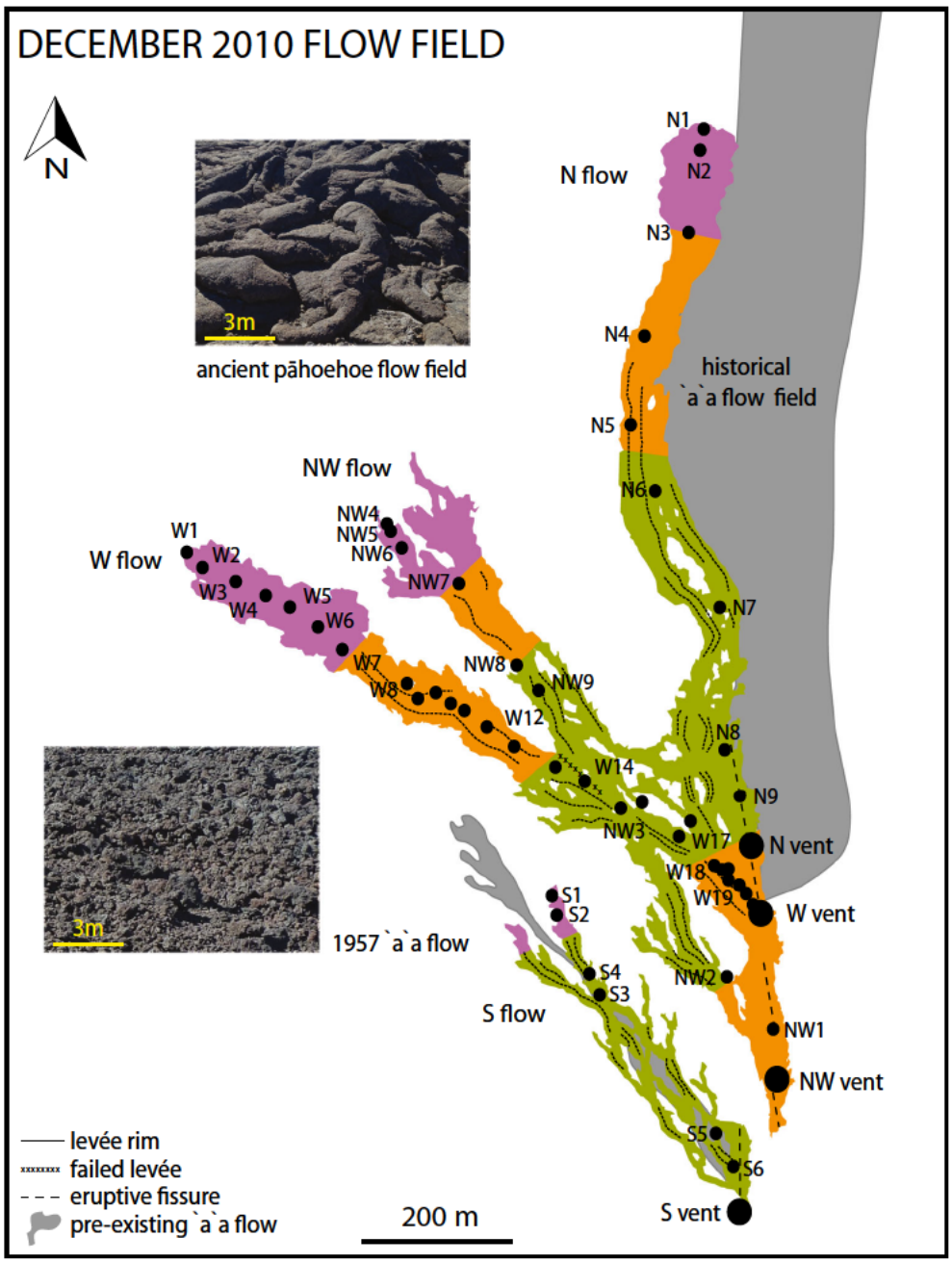


Fig. 3 Structural map of the December 2010 flow field, including eruptive fissures, vents, levée rims, and substrate photos, as well as flow system architecture; sample locations are also plotted. Single channel flow sections are visualized in orange, braided flow sections are displayed in green, and dispersed flow sections are shown in purple

Laboratory-based chemical analyses

The bulk major element composition of lava samples was measured by ICP-AES at the Laboratoire Magmas et Volcans (LMV, Clermont-Ferrand, France). Thin sections were prepared from the upper-most part of the crust of each sample, which was air quenched, thus minimizing post-emplacement crystallization. Analyses were carried out on a Cameca SX100 Electron Microprobe, with operating conditions of 15 kV acceleration voltage, 10 nA beam current, and a 10 μA beam diameter. We obtained around ten glass analyses and five mineral analyses per phase per sample. Glass analytical spots were chosen as far as possible from crystals (at least 20 μm) so that the glass composition would not be affected by crystal growth. The emplacement temperature of the flows was then estimated on the basis of three MgO-based liquid geothermometers: those of Heltz and Thornber (1987), Putirka (2008), and Rhéty et al. (2017). Temperatures were also obtained from three geothermometers based on liquid-mineral equilibrium: liquid-olivine (Putirka et al. 2007), liquid-pyroxene (Putirka et al. 1996), and liquid-plagioclase (Putirka 2005).

Table 1 Sample locations and descriptions

Sample	Easting (UTM 40S) m	Southing m	Elevation m	Vent distance m	Location notes	Description
PF 10S 16 01	365492	7651230	2350	437	Flow center	Spiny ʻaʻā core extrusion
PF 10S 16 02	365511	7651215	2358	413	Inner left levée base	Spiny pāhoehoe
PF 10S 16 03	365526	7651204	2364	396	Central channel	Spiny pāhoehoe extrusion
PF 10S 16 04	365530	7651196	2373	387	Central channel	Spiny pāhoehoe extrusion
PF 10S 16 05	365712	7650931	2466	66	Right levée crest	Pāhoehoe overflow
PF 10S 16 06	365745	7650911	2478	33	Inner left levée	Pāhoehoe overflow
PF 10W 15 01	364994	7651736	2243	934	Flow front extrusion	Spiny Pāhoehoe
PF 10W 15 02	365019	7651718	2251	903	Incipient levée	Up bent slab, deformation levée
PF 10W 15 03	365083	7651693	2257	836	Incipient levée	Up bent slab, deformation levée
PF 10W 15 04	365124	7651661	2261	784	Flow center upwelling	Spiny pāhoehoe
PF 10W 15 05	365153	7651646	2264	752	Flow center overflow	Surface of accreted levée
PF 10W 15 06	365191	7651622	2268	707	Flow center core	Spiny pāhoehoe
PF 10W 15 07	365245	7651578	2271	638	Channel exit center	Spiny pāhoehoe
PF 10W 15 08a	365290	7651542	2280	580	Middle of channel	Slab of spiny pāhoehoe
PF 10W 15 08b	365275	7651516	2284	580	Overflow levée	ʻAʻā margin
PF 10W 15 09	365334	7651511	2292	527	Overflow levée	Rough pāhoehoe/ʻaʻā swirls
PF 10W 15 10	365367	7651500	2303	493	Overflow levée	Rough pāhoehoe/ʻaʻā swirls
PF 10W 15 11	365401	7651492	2309	460	Middle of channel	Spiny rough pāhoehoe
PF 10W 15 12	365429	7651467	2313	423	Middle of channel	Spiny rough pāhoehoe
PF 10W 15 13	365461	7651439	2322	381	Middle of channel	Rough spiny pāhoehoe
PF 10W 15 14	365509	7651423	2326	332	Incipient channel	Downflow spreading cleft
PF 10W 15 15	365550	7651399	2336	285	Middle of channel	Spiny pāhoehoe slab
PF 10W 15 16	365589	7651393	2341	250	Middle of channel	Ooze out of spiny pāhoehoe
PF 10W 15 17	365636	7651360	2355	193	Right levée	Accreted slab of spiny pāhoehoe
PF 10W 15 18	365688	7651326	2366	132	Levée overflow	Spiny pāhoehoe
PF 10W 14 0A	365,787	7651225	2398	9		Spiny pāhoehoe
PF 10W 14 0B	365782	7651242	2392	11		Spiny pāhoehoe
PF 10W 14 01	365765	7651255	2387	28		Spiny pāhoehoe
PF 10W 14 02	365756	7651259	2385	37		Spiny pāhoehoe
PF 10W 14 03	365741	7651272	2382	57		Spiny pāhoehoe
PF 10W 14 04	365729	7651282	2377	72		Spiny pāhoehoe
PF 10W 14 05	365713	7651288	2374	88		Spiny pāhoehoe
PF 10W 14 06	365713	7651288	2374	88		Spiny pāhoehoe
PF 10W 14 07	365706	7651296	2369	98		Spiny pāhoehoe
PF 10W 14 08	365696	7651306	2366	113		Spiny pāhoehoe
PF 10W 14 09	365691	7651310	2363	119		Spiny pāhoehoe
PF 10W 14 10	365676	7651324	2359	140		Spiny pāhoehoe
PF 10NW 16 01	365796	7651006	2462	52	Vent channel exit	Rubbly pāhoehoe overflow
PF 10NW 16 02	365743	7651125	2421	87	Main channel	Spiny pāhoehoe
PF 10NW 16 03	365621	7651343	2353	335	Channel, pre intersection	Spiny pāhoehoe
PF 10NW 16 04	365261	7651782	2251	901	Dispersed flow area	Spiny pāhoehoe surface extrusion
PF 10NW 16 05	365260	7651771	2253	893	Incipient left levée outer rim	Spiny pāhoehoe
PF 10NW 16 06	365284	7651741	2261	855	First well formed levée	ʻAʻā accretion on inner left levée
PF 10NW 16 07	365419	7651650	2292	703	Groove	Spiny pāhoehoe slab
PF 10NW 16 08	365487	7651531	2315	566	Smooth grooved inner wall	Spiny pāhoehoe accreted to left levée
PF 10NW 16 09	365487	7651522	2317	559	Channel	Spiny pāhoehoe
PF 10N 16 01	365709	7652301	2170	1173	Channel extrusion	Spiny pāhoehoe
PF 10N 16 02	365655	7652275	2185	1152	Vertical slab in channel	Spiny pāhoehoe

Table 1 (continued)

Sample	Easting (UTM 40S) m	Southing m	Elevation m	Vent distance m	Location notes	Description
PF 10N 16 03	365659	7652169	2181	1046	Left levée pre slope break	Spiny pāhoehoe
PF 10N 16 04	365631	7652012	2224	895	Steep channel by right levée	Spiny pāhoehoe
PF 10N 16 05	365601	7651899	2265	790	Left levée, gentle slope zone	Spiny pāhoehoe
PF 10N 16 06	365619	7651828	2274	717	Tube exit channel core crack	Spiny pāhoehoe
PF 10N 16 07	365702	7651662	2311	538	Tube exit channel core crack	Spiny pāhoehoe
PF 10N 16 08	365756	7651373	2358	245	Tube exit channel core crack	Spiny pāhoehoe
PF 10N 16 09	365772	7651206	2395	77	Right levée just up the path	Spiny pāhoehoe

Laboratory-based textural analyses

The density of each collected sample was measured following the methodology proposed by Houghton and Wilson (1989) based on the Archimedes principle and the procedure described by Shea et al. (2010), Robert et al. (2014), and Rhéty et al. (2017). The dense rock equivalent (DRE) density was measured in a helium pycnometer and calculated through the Boyle-Mariotte law and has a precision better than 2%.

For each flow, one near-vent sample and one near-toe sample were investigated. The largest vesicle and crystal populations were imaged by scanning both the sectioned sample and the thin section taken from it with a desktop scanner. Digitization of the thin sections was completed both in natural and polarized light using polarized paper placed at different angles with respect to the sample (Pioli et al. 2014). Subsequent higher magnification images were acquired using a scanning electron microscope (SEM). Following Robert et al. (2014) and Rhéty et al. (2017), for each section we collected three images at 25× magnification and six images at 100×. Images were prepared in Adobe Photoshop®, where crystals, vesicles, and glass were each assigned a different gray tone. Phase volume fraction was measured through FOAMS (Shea et al. 2010), a MATLAB-based code that calculates the percentage of each gray tone and therefore of crystals, vesicles, and glass for multiple same-sample images acquired at different magnifications. This method allowed us to account for the crystal and vesicle size range found in each sample, down to a minimum crystal size of 12.5 μm. To compare the crystallinity of different samples, crystallinity values were normalized to the sample-specific dense fraction with the following equation:

$$\phi_{xtals} = \phi_{xtals\ measured}/(1-\phi_{bbl}) \quad (1)$$

where ϕ_{xtals} is the corrected crystallinity, $\phi_{xtals\ measured}$ is the non-corrected crystallinity, and ϕ_{bbl} is the porosity obtained through density measurements.

Based on their size, three types of crystals were identified. Macrocrysts are olivines greater than 0.5 mm in diameter as described by Welsch et al. (2009) for the recent products of Piton de la Fournaise. Mesocrysts are crystals of olivine, clinopyroxene, and plagioclase, between 0.1 and 0.5 mm in diameter. Microcrysts are crystals of olivine, clinopyroxene, and plagioclase less than 0.1 mm in diameter. The total crystallinity values reported in this study only comprise the macrocrysts and the mesocrysts, corresponding to the crystals that formed in the magma reservoir (Welsch et al. 2009), but exclude microcrysts that instead formed in the shallow reservoir and the conduit (Di Muro et al. 2015), as well as during flow emplacement and post-emplacement cooling (Rhéty et al. 2017). All the raw data are available in the DYNVOLC Database (nd).

Results

Flow system dimensions

DEM-based mapping identifies a 0.213-km^2 flow field, subdivided between four flows, one of which (the north-west flow) comprises distinct upper and lower sections. The south flow volume is 0.023 km^2, the west flow volume is 0.065 km^2, the upper north-west volume is 0.016 km^2, the lower north-west flow volume is 0.033 km^2, and the north flow volume is 0.076 km^2. This compares to an overall flow field areal extent of ~0.25 km^2 calculated through Google Earth. The thickness of the flow field (Fig. 1) varies between 0 and 8.6 m, with a mean value of 1.7 m and a median value of 1.5 m. The overall flow volume is calculated to be of 0.35 km^3: 0.022 km^3 for the south flow, 0.126 km^3 for the west flow, 0.018 km^3 for the upper north-west flow, 0.054 km^3 for the lower north-west flow, and 0.131 km^3 for the north flow.

Flow system emplacement

The order of emplacement of the four channel-fed ‘a‘ā flow units can be derived from the thermal camera imagery (Fig. 2). The long line of sight distance, pixel size and atmospheric

effects mean that lava flow temperatures in the thermal imagery (of just 65 °C in the 05:25 image) are low and not representative of the actual surface temperatures. The flows have approximately the shape and dimensions of those mapped in Fig. 1, so that by 05:25 on December 10, it appears that the flow field had reached its full extent. This is consistent with the OVPF eruption bulletin of 06:45 on December 10 that noted that the lava flows were active but with a "weak flux" (Di Muro 2010f). Thus, most of the lava was erupted between 22:40 on December 9 and around 05:40 on December 10, meaning that the TADR over the first 7 h was no more than 20 m^3/s. Of the four flows, the west and north flows were the hottest with image temperatures of up to 85 °C and 76 °C, respectively. While the lower section of the north-west flow had image temperatures of up to 72 °C, the upper section had a maximum image temperature of just 61 °C. Likewise, the south flow was relatively cool at 64 °C. This indicates that, while activity at the west, north, and lower north-west flows was waning at the time of imaging, activity at the upper north-west and south flows had already stopped some time before the image was acquired.

The south flow, 390 m long and oriented ~ N320°, was fed by the highest altitude section of the fissure (Fig. 3). It mostly followed the pre-existing channels of the 1957 flow, so that the December 2010 levées became nested inside the 1957 levées. Near-vent, the channel was 3.2 m wide on a 18° slope, with late stage 'a'ā being 1.4 m below bank and the levées being 1.6 m high. Calculated velocity for initial, full-channel flow was 7.3 m/s, and velocity for late stage flow was 0.1 m/s. Using Jeffreys' equation (Jeffreys 1925), this equates to effusion rates waning from an initial peak of ~ 38 m^3/s to ~ 0.1 m^3/s.

The west flow was 970 m long and oriented ~ N300° (Fig. 3). Its dimensions and emplacement characteristics have already been well described by Rhéty (2014) and Harris et al. (2015), with calculated peak flow velocities of ~ 4.4 m/s in a channel that was 1.4 m deep and 4.5 m wide, on a slope of 14° for a peak effusion rate of ~ 28 m^3/s. Late stage flow in the master channel was around 1 m below the banks, giving a velocity of ~ 0.4 m/s and an effusion rate of ~ 0.6 m^3/s.

The north flow erupted from the lowermost section of the fissure (Fig. 3) and had an orientation of ~ N350°. It followed the margin of the 2000 flow field and attained a final length of 1100 m, being the longest of the four flows erupted during the December 2010 event. Near-vent, the master channel had a width of 4 m. Proximal levée height was 1.5 m, and undrained flow depth was 1.6 m. On a 11° slope, this gives a peak flow velocity of ~ 4.5 m/s, and a calculated peak effusion rate of ~ 29 m^3/s. Late stage flow velocity was ~ 0.02 m/s, which converts to an effusion rate of ~ 0.01 m^3/s.

The north-west flow is oriented ~ N330° and is actually a 830 m-long flow field that can be divided into two segments: upper and lower. The upper segment is a channel-fed 'a'ā flow that is cut by the west flow. The north-west flow has a channel width of around 2 m and depth of 1 m which, down a slope of 14°, gives an estimated velocity of ~ 2.2 m/s and a calculated effusion rate of ~ 5 m/s. We interpret the field evidence as the west flow having established a channel across the path of the upper north-west flow, which then ran into it. This may have contributed to failure down a 30 m length of the right levée of the west flow, which fed the lower segment of the north-west flow. In the lower north-west flow a broad (~ 6 m), shallow (1.5–1.75 m deep), channel developed on a 10° slope, with calculated effusion rates in the range 33–52 m^3/s, about twice as high as for the upper segment. The lower north-west, west, and north flows have similar temperatures in the thermal image (Fig. 2) and therefore appear to have been concurrently active.

Peak effusion rate at the beginning of the eruption was obtained by summing the calculated effusion rates from all four active fissures. This would amount to an initial peak effusion rate of ~ 132 m^3/s just before 23:00 on December 9. This peak effusion rate must have decreased quickly, because by 05:40 on December 10, the TADR for the first 7 h of eruption was no more than 20 m^3/s. This is also consistent with effusion rates during the final phase of effusion of 0.01–0.6 m^3/s.

Flow system architecture

The December 2010 flow field was mainly emplaced over historical inflated pāhoehoe. Pāhoehoe lobe thickness was 0.5–2 m, and lobe width was about 3 m. The exception was the south flow, which was largely emplaced within the 1957 'a'ā channels (Fig. 3). The north-west, west, and north flows all began as single-channel flows (Fig. 4). As the underlying slope decreased, they transitioned to braided flows (Fig. 4). Distally, they reverted to single channels as the slope increased again. Only close to the flow front is flow dispersed (Fig. 4), as is commonly observed at channel-fed flow systems (e.g., Lipman and Banks 1987; Favalli et al. 2010; Rhéty et al. 2017). In this respect, the zone of dispersed flow is a dynamic feature that moves forward as the channel system extends and is then frozen in place when the channelized portion of the system ceases to extend (cf. Rhéty et al. 2017; Favalli et al. 2010). While a flow in extension that has had its supply cut will likely form a single unit (Walker 1972), a flow field that is fed for a longer period of time will likely take on a more complex, compound flow field form (Kilburn and Lopes 1988).

The south flow is braided throughout its length, with 2–4 channels 3–6 m wide, until it rapidly transitions to dispersed flow 45 m before the flow front (Fig. 3). The south flow was emitted by the highest altitude vent at ~ 2470 m a.s.l. It flowed down a steep 18 ± 4° slope for

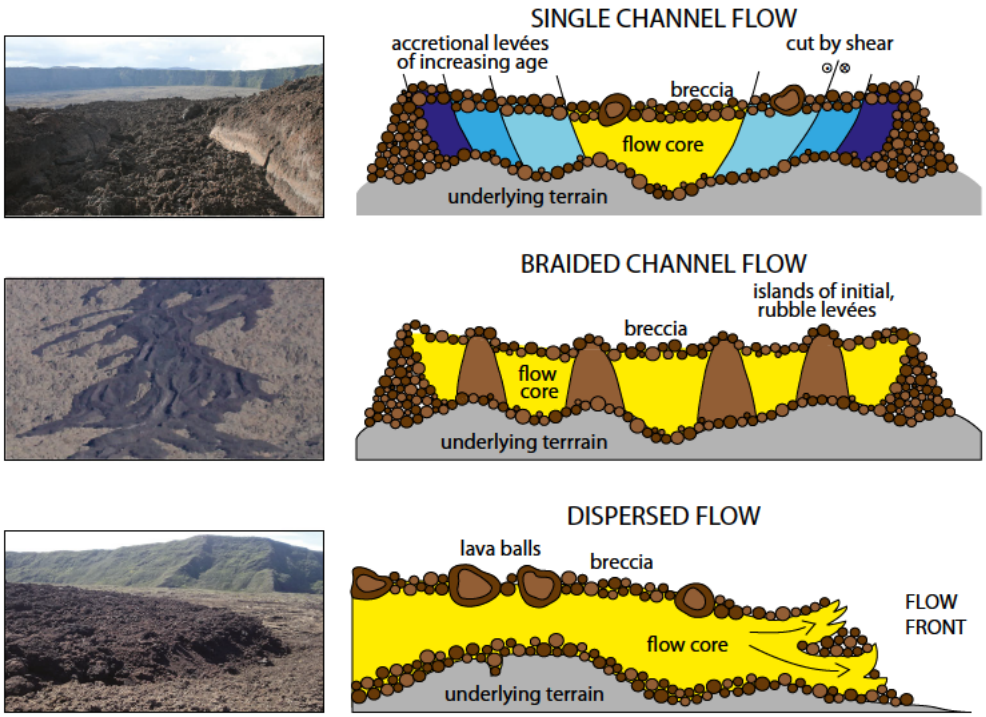


Fig. 4 Flow system architecture typifying photos (left) and cross sections (right): single channel flow transversal cross section view (top panel), braided channel flow transversal cross section view (middle panel), and dispersed flow longitudinal cross section view (bottom panel). The underlying terrain is represented in gray, the flow core is in yellow, the flow levées are in blue, and the breccia and lava balls are in brown. Flow units are typically 1 2 m thick and range in width between 3 and 65 m

350 m. In the proximal area, the main channel is 50 cm deep and 60 cm wide. In the distal area, the main channel is 4 m wide and 65 to 90 cm deep. It is surrounded by two generations of rubble levées, each about 1 m high and having a 25° outward slope. These are the pre-existing levées of the 1957 flow. The final 45 m were emplaced as dispersed flow over a 20 ± 2° slope, where the flow front is about 2 m high and lies just behind the 1957 flow front, which is about 1 m high.

The west flow was erupted from the lower half of the fissure, at around 2390 m a.s.l. It initially ran down a 14 ± 2° slope in a single, narrow (about 4 m wide) channel, before becoming braided after 130 m where the slope is 10 ± 3°. Proximally, the single channel was well defined between initial, rubble levées with near vertical inner walls that were veneered with accreted, fine-grained ʻaʻā striated in the downflow direction. The channel floor is composed of ʻaʻā clasts and slabs of spiney pahoehoe (Fig. 5c). The braided flow has the form sketched in Fig. 4, where the flow unit is bounded by outer initial rubble levées lying on the pre-existing pāhoehoe, and the channels are separated by linear, narrow islands of initial rubble levées that run in and out of the single-channel sections. At 530 m from the vent, the slope steepens again to 11 ± 5°, and the flow reverts to the single-channeled form and morphology. This more distal channel is about 6 m wide and is occasionally bounded by accreted wall slabs displaying downflow striations (Fig. 5c). Up to three generations of deformation levées are recognized along the main channel. At 580 m from the vent, on a slope of 5 ± 2°, the distal channel is defined by incipient shear-defined levées (Fig. 4). Dispersed flow extends about 260 m back from the flow front. The flow front overruns inflated pāhoehoe and tumuli that are 0.5–2 m tall, but lies on the pāhoehoe surface so that the contact can be observed. The flow front height measurement of 2 m is therefore reliable. The flow front is as sketched in Fig. 4 and comprises ʻaʻā clasts and lava balls through which interior lava has extruded as spiny pāhoehoe.

The upper section of the north-west flow was emitted from the fissure just above the west flow vent at an altitude of 2440 m a.s.l. and initially flowed down a 14 ± 4° slope in a single channel (Fig. 5c). The overall width of the flow unit (channel + levées) is about 10 m near the vent. At a distance of 390 m from the vent this channel is cut by the west flow. The lower section of the north-west flow is fed by a breach in the right bank levée of the west flow. Below this, the channel system is braided, where the slope decreases to 9 ± 2°. At this point, the flow unit is 65 m wide. Around 580 m from the vent, the slope increased to 10 ± 2° and the flow reverted to a single-channel form. Where sample NW7 was collected, i.e., ~ 700 m from the vent, there is a broad master channel surrounded by nested rubble levées (Fig. 5b) with spiny pāhoehoe accretions (Fig. 5d). Incipient shear-defined levées are first observed ~ 890 m from the vent, where sample NW5 was collected. At this location, a 15-cm-deep crack associated with shearing at the stream edge separates the levée accreted on the left bank from the main channel (Fig. 5a). Finally, between ~ 930 m from the vent and the flow front, where the slope is 9 ± 1°, the flow is dispersed for 30 m. The flow front is composed of fine-grained ʻaʻā, with sparse pāhoehoe lava boats. The flow front is located in a zone of inflated

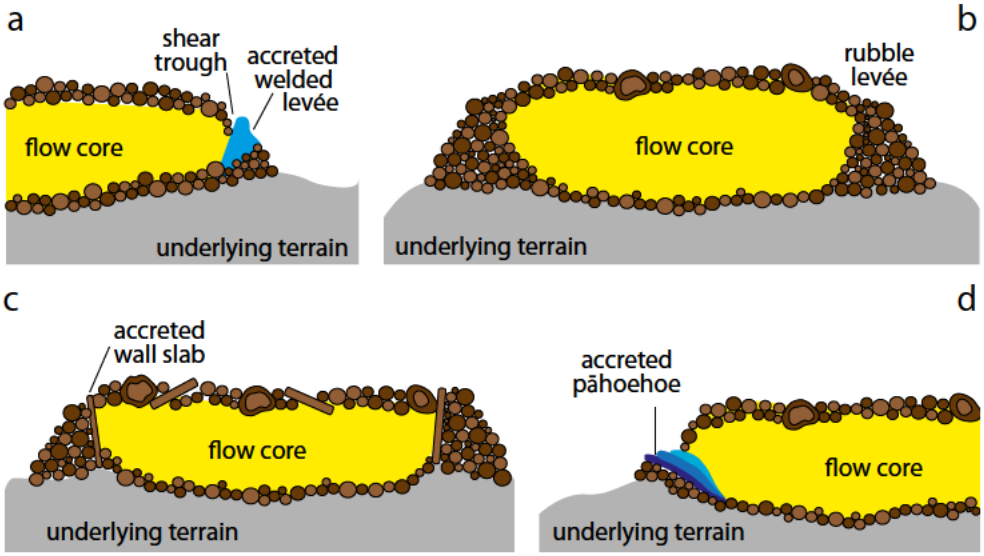


Fig. 5 Cross sections typifying the key features observed in the December 2010 flows: **a** shear troughs and welded levées, **b** rubble levées, **c** accreted wall slabs, and **d** accreted pāhoehoe. Channel depth is typically 1 2 m, while channel width is 3 6 m

pāhoehoe and tumuli that are 0.5–2 m tall. This means that the apparent thickness of the flow front is deceivingly thin (35 cm) because, at this location, the flow front has come to rest in a basin caused by inflation of pāhoehoe around it (Fig. 5b). The basin is 1.75 m deep, and the ‘a‘ā flow front of the north-west flow overtops this by 0.35 m, so the actual thickness of the flow at the front is around 2 m, consistent with the thickness of flow fronts and levée heights elsewhere in the December 2010 lava flow field.

The north flow began as a single channel, emitted from a vent at 2420 m a.s.l. on a 11 ± 4° slope. After 410 m, the slope slightly decreased to 10 ± 3° and the north flow became braided. The surface lava texture is ‘a‘ā throughout, with spiny pāhoehoe accreted internally on to the levée walls (Fig. 5d). At 720 m from the vent, the pre-existing slope steepened to 17 ± 5°, and the braided flow regrouped as a single 20-m-wide channel. At 970 m from the vent, the underlying slope decreased to 2 ± 2° and the flow became dispersed and widened to 85 m (Fig. 3). The flow front is about 2 m high and 25° steep. As the flow front lies over a visible pre-existing pāhoehoe surface, 2 m is the actual flow thickness.

Flow geochemistry and glass geothermometry

The 2010 lava is a tholeiitic basalt (Table 2). Its major element composition is typical of present-day activity of Piton de la

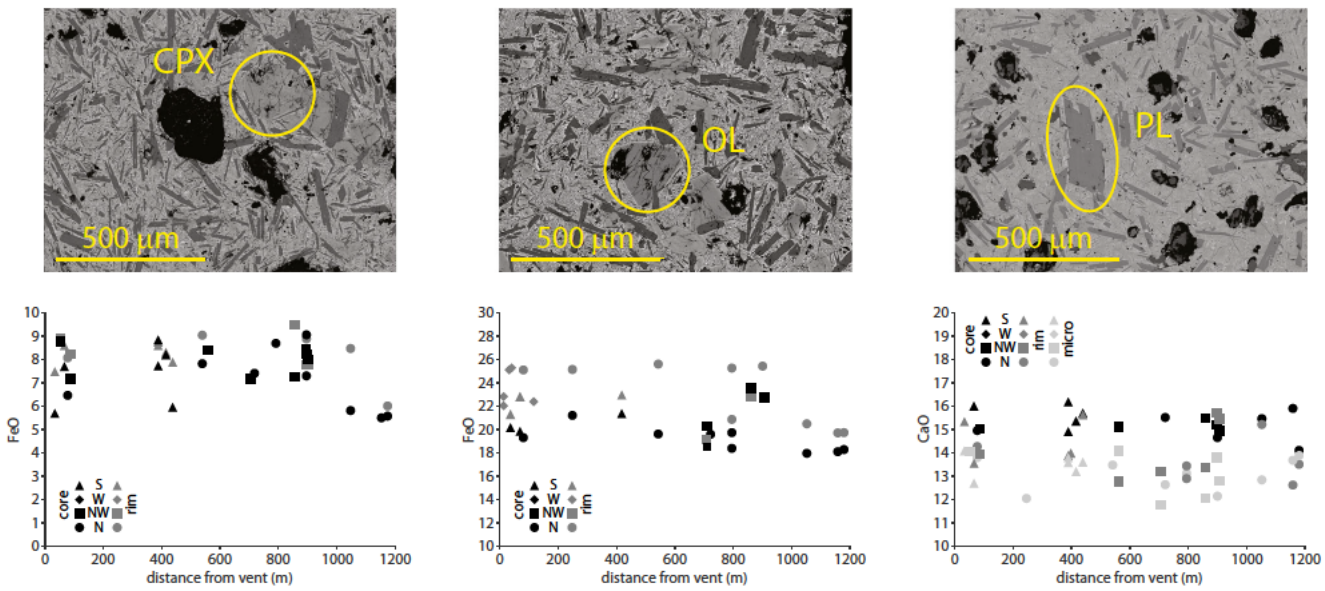


Fig. 6 Upper row: back scattered SEM images exemplifying mineral texture and crystal morphology (CPX = clinopyroxene, sample NW06; OL = olivine, sample NW08; PL = plagioclase, sample NW01). Lower row: geochemical data for each mineral phase plotted against distance from the vent. Black symbols indicate core analyses, dark gray symbols indicate rim analyses, and light gray symbols indicate microlites analyses. Analyses from the south flow are plotted as triangles, from the west flow as diamonds, and from the north west flow as circles

Fournaise, falling within the steady-state basalts (SSB) group, defined by Albarède et al. (1997) as containing 5–8 wt% MgO, 0.5–1 wt% K_2O, and 10–12 wt% CaO. Steady-state basalts have historically erupted at Piton de la Fournaise during low-volume eruptions occurring within the Enclos Fouqué (Albarède et al. 1997), as was the case for the December 2010 event.

To estimate emplacement temperatures and cooling rates down channel, we applied a selection of geothermometers to microprobe analyses of residual glass and minerals of the collected samples (Supplementary Tables 2, 3, 4, and 5; Fig. 6). Clean glass was found in a total of nine samples from all four flow branches. Temperatures obtained with the Rhéty et al. (2017) liquid geothermometer are 1145 ± 10 °C at the vent, compared to 1134 ± 10 °C obtained with the Helz and Thornber (1987) liquid geothermometer, and 1124 ± 60 °C given by the Putirka (2008) liquid geothermometer (Fig. 7). Liquid-olivine (Putirka et al. 2007), liquid-pyroxene (Putirka et al. 1996), and liquid-plagioclase (Putirka 2005) geothermometers, based on mineral-liquid equilibrium, are mostly mutually consistent, indicating temperatures of 1127 ± 60 °C for liquid-olivine to 1158 ± 60 °C for liquid-pyroxene (Fig. 7). The average cooling rate inferred from the comparison of all geothermometers used is 13 °C/km, with individual geothermometers giving values between ~ 11 and ~ 27 °C/km. Data points from different flow branches all lie on the same cooling trend. The eruptive temperature ranges, as inferred from considering samples collected less than 100 m from the vent, are between 1120 and 1160 °C, depending on the considered geothermometer. Because the Rhéty et al. (2017) geothermometer was calibrated specifically on Piton de la Fournaise lavas, we favor a likely eruptive temperature of 1145 ± 10 °C.

Table 2 Representative LA ICP AES bulk rock major elements analyses

Analyte	PF 10W 14 0A	2σ	PF 10W 14 0B	2σ
SiO_2	49.10	0.34	49.10	0.34
Al_2O_3	14.49	0.30	14.44	0.30
Fe_2O_3	12.12	0.01	12.16	0.01
MgO	6.64	0.08	6.66	0.08
CaO	11.35	0.04	11.39	0.04
Na_2O	2.67	0.12	2.54	0.12
K_2O	0.76	0.06	0.79	0.06
TiO_2	2.76	0.10	2.77	0.10
MnO	0.17	0.00	0.17	0.00
P_2O_5	0.32	0.01	0.33	0.01
H_2O^+	0.11		0.12	
H_2O	0.56		0.57	
Total	101.05		101.05	

Textural analyses

Macrocryst and mesocryst contents (Table 3; Fig. 8) are higher at the vent (50–70 vol%) than at the toe (~ 40 vol%) for the north and north-west flows, as has been observed for other lava flow systems at Piton de la Fournaise (Peltier et al. 2009, Rhéty et al. 2017). Conversely, the south flow displays a low crystallinity at the vent (~ 10 vol%), which increases dramatically at the flow front (~ 70 vol%). The west flow also displays a (more modest) crystallinity increase from 45 vol% at the vent to 55 vol% at 132 m from the vent. Density-derived porosity (Table 3) decreases from 55 to 18 vol% from vent to toe, at a steady rate of increase of ~ 3 vol% per 100 m. Data from all four flow branches plot along the same trend, regardless of whether the local flow system architecture consists of a single channel, braided channels, or dispersed flow (Fig. 9). Thus, there appears to be no direct textural (and hence rheological) control on channel architecture.

Discussion

At the onset of the eruption, all vents along the fissure were probably active simultaneously. The south vent, at the highest elevation on the fissure, had the highest calculated peak effusion rate of 38 m^3/s. The west, upper north-west, and north flows had calculated peak effusion rates of 28, 5, and 29 m^3/s which sum to a total initial effusion rate from the fissure as a whole of around 96 m^3/s. However, activity was short-lived, with the entire flow field system being constructed in just 7 h. During this time, all four main flow fields (and hence channel systems) were active simultaneously, although the south and north-west vents shut down some time before the west and north vents. However, the four channel systems were fed at waning rates, where effusion rates are estimated to have been as low as ~ 0.01 m^3/s late in the eruption, so that the TADR for these first 7 h was as high as 20 m^3/s. The short duration of supply and its rapidly waning character is reflected in the simplicity of the channel and levée systems and their morphology, as well as the short length of the flow units. Outer levées are of the simple, rubble type. They have not been modified by increases in lava supply, which would have built overflow levées and led to compound forms. Instead, a single, short opening phase emplaced a single, simple set of levées that defined the channel down which all following lava flowed (Fig. 5c). Fluxes then steadily diminished, as we see no level markers consistent with the flow resting at a certain level for a period of time, but rather an even accretion of a single lava layer to the levée inner walls. Likewise, channel widths steadily decreased by accretion of nested levées whose stagnation and separation from downflowing lava was marked by shear lines

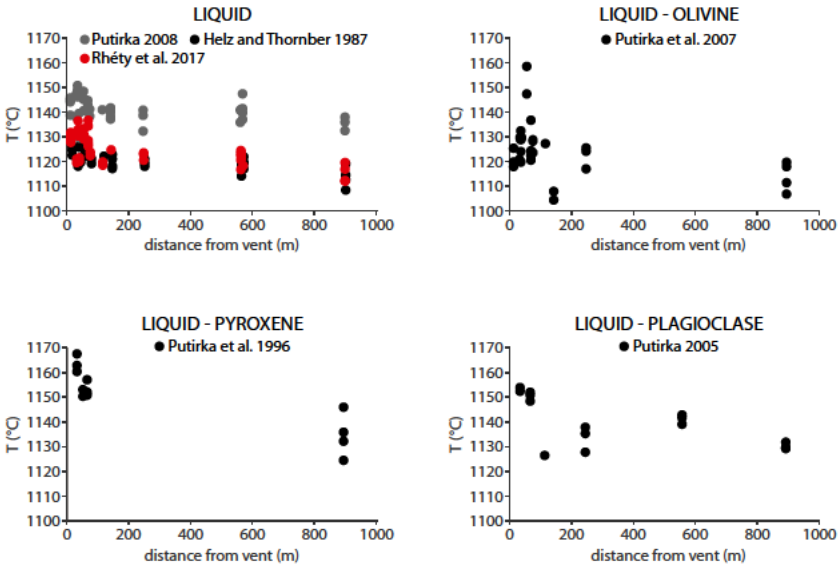


Fig. 7 Emplacement temperatures of each sample obtained through geothermometry. Geothermometers based on liquid MgO content (Helz and Thornber 1987 in black; Putirka 2008 in gray; Rhéty et al. 2017 in red), liquid olivine equilibrium (Putirka et al. 2007), liquid pyroxene equilibrium (Putirka et al. 1996), and liquid plagioclase equilibrium (Putirka 2005)

(Fig. 4). There was, however, downflow variation in the architecture of the channel network. The structure of the channel network thus varied with distance, rather than time, and that variation appears to be linked to the interaction of the lava with the underlying slope.

Slope and flow system architecture

We extracted underlying terrain slope from the pre-eruptive DEM every 1 m and then averaged it every 10 m and every 25 m to better highlight slope trends at different spatial scales (Fig. 10). Averaging pre-existing terrain slope within flow sectors characterized by different channel network architecture as observed in the field, overall slope differences became evident (Fig. 10). The architecture of each flow branch evolves as lava flows over different underlying slopes, alternating between a single channel on steeper slopes and braided channels on shallower slopes. This proves that changes in the architecture of the flow are reversible and that the flow can indeed switch back and forth between single and braided channel configurations multiple times during its emplacement. We developed a regime diagram (Fig. 11) that assesses the transition between single and braided channel flow independently of absolute slope values, but rather as a function of slope change with respect to the upflow section. This regime diagram shows that, for this flow field, the transition from braided to single channel always corresponds to a slope increase, whereas the transition from single to braided channel always corresponds to a slope decrease. Just behind the flow front, flow is always dispersed, with a single or braided channel network developing behind it depending on slope. We conclude that the key parameter controlling whether a channel system is merging or branching is the underlying slope variation.

The south flow appears to violate this rule. The entire south flow pathway is much steeper than that of the three other flows. Our observations suggest that a steeper slope favors a single channel configuration. Instead, the south flow begins as a braided flow and remains such throughout its length, until it becomes dispersed close to the flow front, on a 20° slope (Fig. 10). This can be explained by considering the pre-existing topography underlying the December 2010 flow field (Fig. 3). Whereas the north, north-west, and west flows were emplaced over ancient pāhoehoe flow fields, the south flow was emplaced within the 1957 channel-fed ʻaʻā flow field and re-used its braided channel network. Channel re-utilization exerts a first-order control on flow system architecture. In a case where the pre-existing system has internal relief that is of the same scale (or greater) than the new system, the new channel system will develop within the pre-existing channel system and will thus inherit the channel network of the pre-existing system irrespective of underlying slope. The other three flows studied here were all emplaced over the same ancient pāhoehoe flow field, which had a vertical scale of relief that was less than the new flow thickness (about 2 m). In these cases—channel-fed ʻaʻā flows emplaced on a smooth surface—slope breaks exert the main control on determining whether the channel system is braided or not, as summarized by our regime diagram (Fig. 11).

Comparison with previous studies

The transition from a single flow channel to multiple braided channels can originate from a variety of phenomena, including topographic confinement (Dietterich and Cashman 2014),

Table 3 Sample crystallinity and porosity

Sample	Vent distance m	Crystallinity[a] %	Porosity[b] %
PF 10S 16 01	437	41	41
PF 10S 16 02	413		45
PF 10S 16 03	396		37
PF 10S 16 04	387		36
PF 10S 16 05	66		52
PF 10S 16 06	33	50	50
PF 10W 15 01	934		23
PF 10W 15 02	903		25
PF 10W 15 03	836		27
PF 10W 15 04	784		26
PF 10W 15 05	752		31
PF 10W 15 06	707		39
PF 10W 15 07	638		26
PF 10W 15 08a	580		35
PF 10W 15 08b	580		35
PF 10W 15 09	527		30
PF 10W 15 10	493		49
PF 10W 15 11	460		45
PF 10W 15 12	423		45
PF 10W 15 13	381		41
PF 10W 15 14	332		27
PF 10W 15 15	285		36
PF 10W 15 16	250		38
PF 10W 15 17	193		41
PF 10W 15 18	132	55	35
PF 10W 14 0A	9	45	63
PF 10W 14 0B	11		64
PF 10W 14 01	28		55
PF 10W 14 02	37		55
PF 10W 14 03	57		45
PF 10W 14 04	72		67
PF 10W 14 05	88		65
PF 10W 14 06	88		63
PF 10W 14 07	98		24
PF 10W 14 08	113		36
PF 10W 14 09	119		63
PF 10W 14 10	140		57
PF 10NW 16 01	52	52	65
PF 10NW 16 02	87		46
PF 10NW 16 03	335		41
PF 10NW 16 04	901	44	44
PF 10NW 16 05	893		48
PF 10NW 16 06	855		51
PF 10NW 16 07	703		33
PF 10NW 16 08	566		45
PF 10NW 16 09	559		40
PF 10N 16 01	1173	40	21
PF 10N 16 02	1152		23
PF 10N 16 03	1046		23
PF 10N 16 04	895		24
PF 10N 16 05	790		26
PF 10N 16 06	717		35
PF 10N 16 07	538		32
PF 10N 16 08	245		37
PF 10N 16 09	77	68	34

[a] Crystallinity is reported as % of dense rock material

[b] Porosity is calculated on the basis of density measurements

flow front interaction with topographic obstacles (Dietterich et al. 2015), levée breakouts and overflows, and possibly flow front fingering (Huppert 1982). Hereafter, we consider the case of a flow that is not topographically confined, but interacts with an obstacle. If the amplitude of the underlying topographic roughness is comparable to that of the flow front, it acts as an obstacle, causing the flow to braid. Obstacles decrease flow momentum by exerting a drag on it. At low effusion rate, and consequently low velocity and low momentum, the flow front will be more affected by the momentum decrease imposed by the obstacle and will braid in response. Conversely, a high-effusion, high-velocity flow may have the kinetic energy necessary to overcome the obstacle unaffected (Soule et al. 2004). Lava flows characterized by low effusion rates should therefore be more prone to braiding compared to high effusion rate flows on any given slope. However, when encountering a slope decrease, lava will momentarily slow down, leading to a lava backup. Such lava accumulation will result in an increase in the flow front amplitude, which will allow the previously braided flow to converge into a single-channel flow. This scenario is supported by the experimental study of Dietterich et al. (2015), which shows that flows become thicker in proximity of an obstacle, producing a bow wave that can overcome the obstruction prompting its formation. Furthermore, faster flows produce higher bow waves (Dietterich et al. 2015). Since flow speed is directly proportional to slope (for any given effusion rate), lava flowing down a steeper slope will thicken more when interacting with a topographic obstacle, and as a result, it will be more likely to overcome it, continuing to flow in a single channel (Dietterich et al. 2015). This directly applies to the studied flow field, whose underlying slopes are very steep, resulting in high calculated flow velocities, of up to ~8.5 m/s. This may explain the architectural difference between thin near-vent pāhoehoe sheet flows, that will likely flow into an

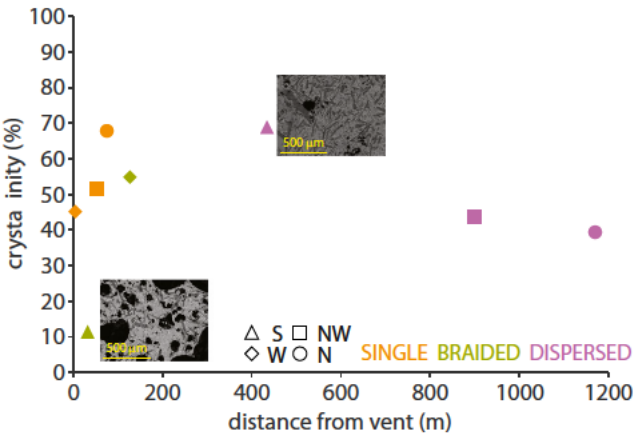


Fig. 8 Crystallinity of vent and toe samples of each flow. Analyses from the south flow are plotted as triangles, from the west flow as diamonds, from the north west flow as squares, and from the north flow as circles. Samples collected within single channel flow sections are visualized in orange, samples collected in braided flow sections are displayed in green, and samples from dispersed flow sections are shown in purple. The two inset images illustrate the vent to toe (vent sample: S06; toe sample: S01) textural evolution of the south flow

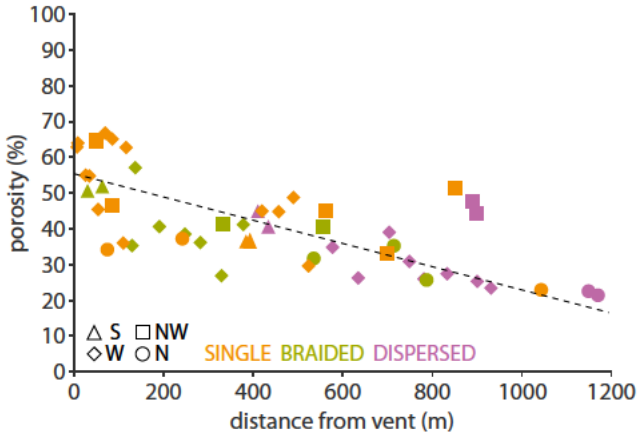


Fig. 9 Porosity trend of all collected samples. Analyses from the south flow are plotted as triangles, from the west flow as diamonds, from the north west flow as squares, and from the north flow as circles. Samples collected within single channel flow sections are visualized in orange, samples collected in braided flow sections are displayed in green, and samples from dispersed flow sections are shown in purple

increasingly small number of channels, and thick ‘a‘ā flows that will likely begin as a well-defined channel and later braid on shallower slopes where flow stalls and spreads so as, in the ultimate case, to form perched ponds (Parfitt et al. 1993).

Our observation of steeper slopes favoring channel confluence and gentler slopes favoring channel divergence contrasts with the observations of Dietterich and Cashman (2014) at Mauna Loa, Rhéty et al. (2017) at Piton de la Fournaise, and Krauskopf (1948) at Paricutín. Effusion rate does not appear to explain the differences between our results and previous studies. The Mauna Loa flows analyzed by Dietterich and Cashman (2014) were fed at a rate > 100 m^3/s, and we calculate that the Piton de la Fournaise flows considered in this study had an initial peak effusion rate of ~120 m^3/s, although they must have rapidly waned to much lower rates of < 20 m^3/s. Rhéty et al. (2017) report that the 2007 lava contained 43–60 vol% of olivine macrocrysts (3–4 mm in diameter), whose content (indicative of effusion rate), varies throughout the system, increasing downflow (as the first lava emplaced has the highest transport capacity, and hence the highest macrocryst bedload). This suggests an initially high effusion rate, responsible for emplacing the distal macrocryst-rich lava, and therefore, the effusion history of this flow closely resembles the 2010 eruption. Therefore, the discrepancy between the flow system architecture observed at Mauna Loa and Piton de la Fournaise in 2007, and that observed in this study at Piton de La Fournaise in 2010, cannot be explained solely in terms of differences in effusion rate, suggesting that a

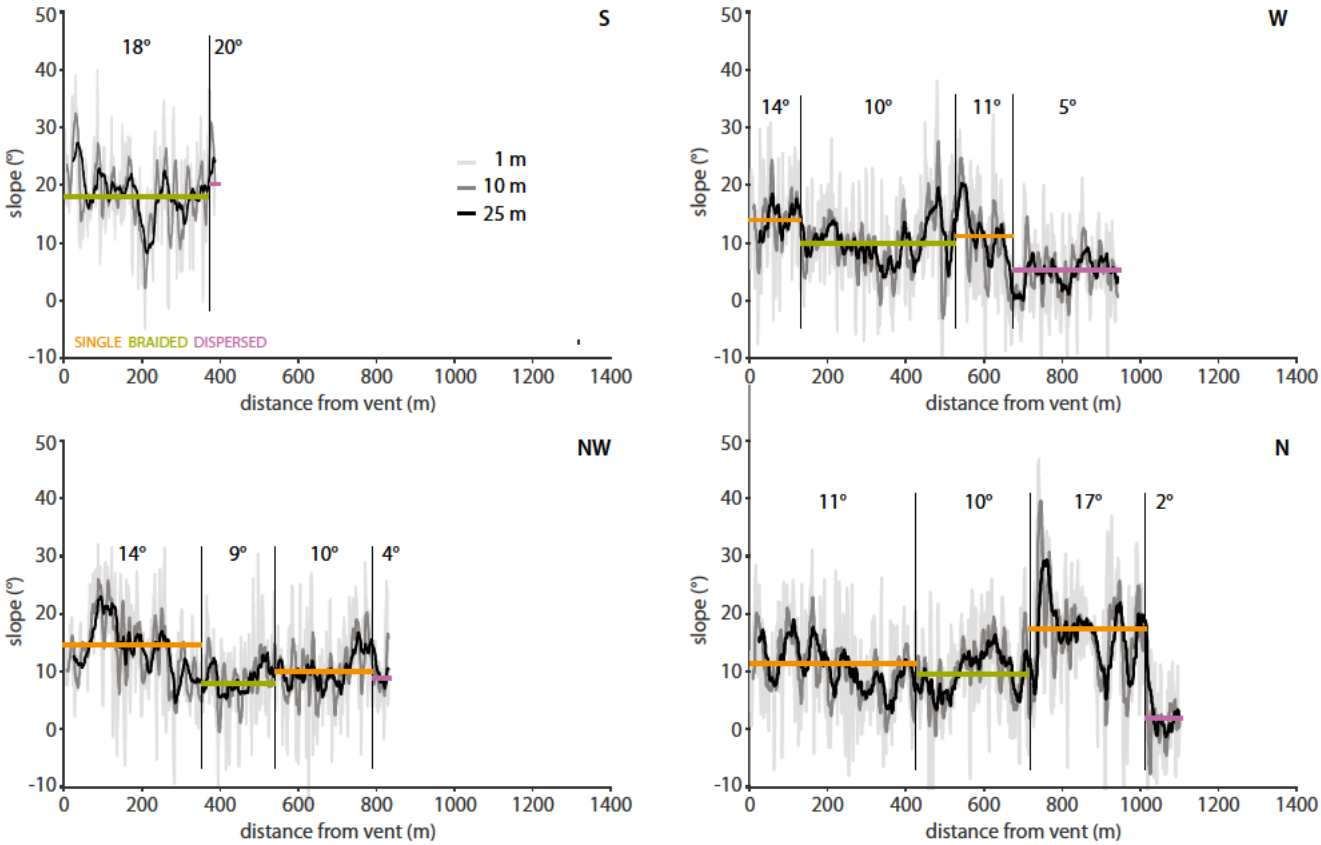


Fig. 10 Pre eruptive substrate slope variations for each flow: every 1 m (light gray), averaged over 10 m (dark gray), averaged over 25 m (black). Section averages are superimposed and color coded according to flow system architecture: single channel flow in orange, braided flow sections in green, and dispersed flow in purple

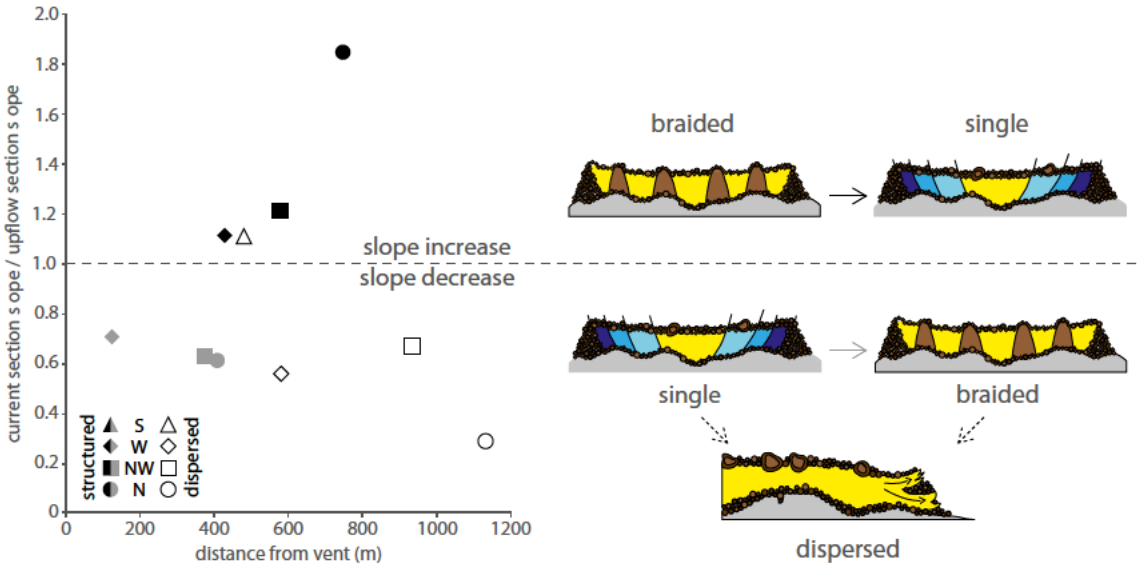


Fig. 11 Flow system architecture regime diagram. Values of the ratio between the averaged pre eruptive slope of the current and upflow sec tions above 1 signify a slope increase, whereas values below 1 signify a slope decrease. Analyses from the south flow are plotted as triangles, from the west flow as diamonds, from the north west flow as squares, and from the north flow as circles. Black symbols represent transitions from braided to single channel flow, gray symbols from single to braided flow, and white symbols from either single or braided to dispersed flow. Sketches dimensions are as in Fig. 4

further careful study of other parameters, such as emplacement conditions and textural parameters, is necessary.

While the study of Dietterich and Cashman (2014) and ours both focused on ʻaʻā flows, that of Rhéty et al. (2017) examined a pāhoehoe sheet flow that became organized into channels that then turned into ʻaʻā. The crystallinity of Mauna Loa lavas is generally quite low, with a phenocryst content of less than 0.5 vol% and a variable microphenocryst content of up to 30 vol% (Lipman and Banks 1987), whereas Piton de la Fournaise lavas crystallize microlites in the shallow reservoir and during ascent in the conduit, leading to a high total crystallinity of up to 70 vol%. Importantly, the study of Rhéty et al. (2017) focuses on oceanites, whose olivine crystal size vastly exceeds the crystal size range considered in our study. Analogue studies such as Del Gaudio et al. (2013) show that crystal size critically affects the rheological behavior of lava. Porosity values appear consistent across the two Mauna Loa and Piton de la Fournaise volcanic systems, although at Piton de la Fournaise porosity decreases more rapidly with increasing distance from the vent. Downflow variations in crystallinity and porosity are not expected to affect the applicability of our results, as we showed that their variation has apparently no effect on flow system structure for the 2010 eruption of Piton de la Fournaise (Fig. 8).

Effect of textural parameters

Most previous studies on the surface morphology and the texture of basaltic lava flows focused on cooling-limited Hawaiian lava flows (Lipman and Banks 1987; Moore 1987; Crisp et al. 1994; Cashman et al. 1999; Riker et al. 2009; Robert et al. 2014). The thermal history of such flows is determined by the rate of heat loss from the surface through both radiation and convection and from the base through conduction (Keszthelyi and Denlinger 1996), as well as by the entrainment of colder material (Crisp and Baloga 1994), all of which is modulated by the release of latent heat of crystallization (Crisp et al. 1994; Keszthelyi and Denlinger, 1996). Cashman et al. (1999) noted that once the thermal profile of the flow becomes stratified, the surface morphology transitions from pāhoehoe to ʻaʻā, starting at the channel edges and moving inward. The variation of rheological parameters, in particular the onset and development of yield strength associated with flow crystallization, also contributes to the morphological transition incurred by lava flows (Peterson and Tilling 1989; Sehlke et al. 2014). These factors all contribute to controlling flow regime and morphology (e.g., Harris and Rowland 2001; Soule et al. 2004; Favalli et al. 2018). Glaze et al. (2014) noted that slope breaks in the terrain underlying lava flows can create eddies that disrupt the flow surface, enhancing radiative heat loss and thus reducing the distance the flow can travel. However, for the highly crystalline lava emplaced during the 2010 Piton de La Fournaise eruption, this effect would be minor. Indeed, we do not find any evidence of abrupt cooling and increased crystallization immediately after slope breaks.

Crystallinity and porosity were analyzed for all flow branches to identify any possible relation to flow system architecture. Comparison of thin sections of samples collected in differently structured areas of the flow shows no systematic variation in crystal content, indicating that crystallinity evolution does not control flow structure. The observed pre-

emplacement crystallinity trends (Fig. 8), increasing from vent to toe for the south and west flows, and decreasing from vent to toe for the north-west and north flows, have been interpreted to reveal variations in effusion rate where, as the effusion rate increases, so too does the transport capacity of the lava so that higher crystal loads can be carried at higher effusion rates (e.g., Rhéty et al. 2017; Hammer et al. 2000, Noguchi et al. 2008). According to this interpretation, the eruption began along the entire fissure, but different segments erupted at different effusion rates. Indeed, the highest crystal contents are observed at the vents for which effusion rate was calculated to be highest. For example, at the south vent, peak effusion rates of ~ 44 m^3/s were capable of mobilizing lava containing 70 vol% crystals and to carry it to the distal portion of the system, revealing that it was the first lava emitted. At other vents, where effusion rates were lower, the carrying capacity was lower. At the west and north-west flows, peak effusion rates were between ~ 10 and ~ 30 m^3/s, thus carrying a lower crystal load at peak flow of 40–50 vol% crystals. As effusion rates waned, so too did the carrying capacity. For example, in the final stage of effusion at the south flow, effusion rates waned to ~ 0.1 m^3/s, and the crystal cargo declined to 10 vol%. Thus, near-vent we find the final, low crystallinity lava erupted at the lowest effusion rate as activity at the vent waned. In other flows, near-vent crystallinities of 50–70 vol% (Fig. 8) likely indicate that magma was extracted from a heterogeneous, stratified magma chamber, with the crystal-rich material from the base of the shallow reservoir being erupted last (Gurioli et al. 2018).

In comparison, the 2007 flow of Piton de la Fournaise (Rhéty et al. 2017) has a near-vent crystallinity of 55 vol%, increasing to 75 vol% at the flow front due to microlite crystallization. The 1974 Mauna Ulu flow (Robert et al. 2014) has a crystallinity of 15 vol% near the vent, increasing to 45 vol% 6 km from the vent. In this case, the crystallinity increase is due to the incremental crystallization of microlites, whereas the phenocryst content remains stable, suggesting a constant mass eruption rate (Robert et al. 2014).

For the December 2010 eruption, sample porosity decreases uniformly with distance from the vent, regardless of whether the analyzed samples belong to a single-channel, braided, or dispersed section of the flow (Fig. 9). As a result, there is no correlation between flow system architecture and sample porosity. In comparison, the 2007 flow of Piton de la Fournaise as analyzed by Rhéty et al. (2017) shows a uniform trend of decreasing porosity along both flow channels considered, comparable in magnitude to that observed here. The 1974 Mauna Ulu flow (Robert et al. 2014), which maintained a single-channel structure throughout its length, also shows a porosity decrease with increasing distance from the vent, although it is less pronounced than at Piton de la Fournaise.

Appraisal of these three cases (Piton de la Fournaise 2007 and 2010 and Mauna Ulu 1974) highlights that downflow trends in temperature, crystallinity, and porosity are the same for single and braided channel cases. Additionally, the case of the 2010 flow field of Piton de la Fournaise reveals that temperature, crystallinity, and porosity trends are uninterrupted across transitions between single and multiple channel flow. This supports a model within which cooling rate is depth-dependent, but independent of channel width (cf. Harris and Rowland 2001, 2009).

Soldati et al. (2016) showed that changes in flow velocity across breaks in slope can be larger than would be predicted for example through Jeffreys' equation (Jeffreys 1925). This is due to the non-Newtonian behavior of multi-phase lava, which results in non-linear flow velocity variations that amplify the effect of even modest slope changes. For example, a steeper slope exerts a greater stress on the flowing lava, resulting in a faster flow velocity. Since lava is shear-thinning, a greater stress results in a lower effective viscosity (which would not happen for a Newtonian fluid). In turn, this lower effective viscosity causes velocity to increase, more so than it would for a Newtonian fluid. Because deviation from Newtonian behavior increases with crystallinity (Ryerson et al. 1988), this effect will be more pronounced in highly crystalline lavas, such as those investigated in this study, as opposed to less crystalline ones.

Implications

Flow system architecture has fundamental implications well beyond flow morphological appearance. For any given lava effusion rate at the vent, the same supplied flux can feed either one large channel, or may be divided among multiple smaller channels. As a result, for any given supplied flux a single channel system will have a higher volumetric flux than each branch of an equivalent braided channel system. The increased viscous drag imposed by the larger wetted perimeter of a braided system will result in decreased flow speed and, consequently, length. This is in accordance with the supply rate rule (Walker et al. 1973) and with mass-energy analysis (Tarquini, 2017). Conversely, the transition from braided channels to a single channel will increase the flow speed and length, as demonstrated by Dietterich and Cashman (2014).

If channel depth remains constant through the transition from single channel to braided channels, velocity and cooling rate will also remain constant, as will the cooling-limited flow length (Rhéty et al. 2017). Conversely, if partitioning the flux diminishes flow depth (Lister 1992), then, holding all else constant, velocity will decrease and cooling rate will increase (Harris and Rowland 2001), hence reducing the cooling-limited flow length. If the flow depth remains constant (as in the case analyzed here) then models become depth-independent. As a result, cooling-related models become

unaffected by partitioning (division between multiple branches) of a control volume, so that simple 1-D models, such as FLOWGO (Harris and Rowland 2001) and MOLASSES (Richardson 2016), that assume flow depth remains approximately constant downflow, apply.

Conclusion

Slope variations have a primary influence over channel network architecture (e.g., Krauskopf 1948; Dietterich and Cashman 2014; Rhéty et al. 2017). On the basis of our data, we here develop a regime diagram that places the channel network architecture of relatively low effusion rate lava flows in a dynamic setting. However, this regime diagram cannot be applied universally, as counter-examples exist in the literature for different effusion rates, compositions, and textures.

We found that changes in the crystal and bubble content do not correlate with changes in the number of channels, implying that these textural parameters do not exert a direct control on channel network architecture. However, we know from previous studies that pre-existing topography can strongly affect the apparent viscosity of lava flows due to their non-Newtonian behavior (e.g., Peterson and Tilling 1980; Lev and James 2014; Soldati et al. 2016) and that crystal and bubble contents affect the degree of non-Newtonian behavior of lava (e.g., Costa et al. 2009; Llewellin et al. 2002; Mader et al. 2013). Both morphological and rheological perspectives remain therefore necessary to fully characterize a channel-fed flow system and to adequately model its development.

Acknowledgements We wish to thank the reviewers, E. Rumpf and S. Tarquini, the Editor, H. Dietterich, and the Deputy Executive Editor, J. Taddeucci, for their constructive feedback.

Funding information This research was funded by National Geographic Young Explorer grant #9817 15 to A.S. and Chateaubriand STEM Fellowship of the Office for Science and Technology of the Embassy of France in the United States to A.S. This research was also supported by the National Science Foundation grant EAR 1220051 to AW. The field work of L.G. in 2013 was supported by the "Action Incitative_2013" of OPGC. We thank the STRAP project funded by the Agence Nationale de la Recherche (ANR 14 CE03 0004 04). This research was financed by the French Government Laboratory of Excellence initiative no. ANR 10 LABX 0006, the Région Auvergne, and the European Regional Development Fund. This is Laboratory of Excellence Clervolc contribu tion number 310.

References

Albarède F, Luais B, Fitton G, Semet M, Kaminski E, Upton BG, Bachèlery P, Cheminée JL (1997) The geochemical regimes of Piton de la Fournaise volcano (Réunion) during the last 530 000 years. J Petrol 38(2):171 201. https://doi.org/10.1093/petroj/38.2.171

Bachèlery P, Lénat JF, Di Muro A, Michon L (2016), Active volcanoes of the Southwest Indian Ocean: Piton de la Fournaise and Karthala. Active volcanoes of the world. Springer Verlag, Berlin and Heidelberg 1 428. https://doi.org/10.1007/978 3 642 31395 0_12

Bailey JE, Harris AJ, Dehn J, Calvari S, Rowland SK (2006) The chang ing morphology of an open lava channel on Mt. Etna. Bull Volcanol 68(6):497 515

Cashman KV, Thornber C, Kauahikaua JP (1999) Cooling and crystalli zation of lava in open channels, and the transition of Pāhoehoe lava to 'a'ā. Bull Volcanol 61(5):306 323. https://doi.org/10.1007/s004450050299

Coppola D, Villeneuve N, Di Muro A, Ferrazzini V, Peltier A, Favalli M, Bachèlery P, Gurioli L, Harris A, Moune S, Vlastélic I, Galle B, Arellano S, Aiuppa A (2017) A shallow system rejuvenation and magma discharge trends at Piton de la Fournaise volcano (La Réunion Island). Earth Planet Sci Lett 463:13 24. https://doi.org/10.1016/j.epsl 2017.01.024

Costa A, Caricchi L, Bagdassarov N (2009) A model for the rheology of particle-bearing suspensions and partially molten rocks. Geochem Geophys 10(3)

Crisp J, Baloga S (1994) Influence of crystallization and entrainment of cooler material on the emplacement of basaltic 'a'ā lava flows. J Geophys Res Solid Earth 99(B6):11819 11831. https://doi.org/10.1029/94JB00134

Crisp J, Cashman KV, Bonini JA, Hougen SB, Pieri DC (1994) Crystallization history of the 1984 Mauna Loa lava flow. J Geophys Res Solid Earth 99(B4):7177 7198

Del Gaudio P, Ventura G, Taddeucci J (2013) The effect of particle size on the rheology of liquid solid mixtures with application to lava flows: results from analogue experiments. Geochem Geophys Geosyst 14(8):2661 2669. https://doi.org/10.1002/ggge.20172

Di Muro A (2010a) Bulletin Volcanologique du 09 Décembre. Daily Bulletin of the Observatoire Volcanologique du Piton de la Fournaise, 9 December 2010, OVPF_20101209_1

Di Muro A (2010b) Bulletin Volcanologique du 09 Décembre. Daily Bulletin of the Observatoire Volcanologique du Piton de la Fournaise, 9 December 2010, OVPF_20101209_2

Di Muro A (2010c) Bulletin Volcanologique du 09 Décembre. Daily Bulletin of the Observatoire Volcanologique du Piton de la Fournaise, 9 December 2010, OVPF_20101209_3

Di Muro A (2010d) Bulletin Volcanologique du 09 Décembre. Daily Bulletin of the Observatoire Volcanologique du Piton de la Fournaise, 9 December 2010, OVPF_20101209_5

Di Muro A (2010e) Bulletin Volcanologique du 09 Décembre. Daily Bulletin of the Observatoire Volcanologique du Piton de la Fournaise, 9 December 2010, OVPF_20101209_6

Di Muro A (2010f) Bulletin Volcanologique du 10 Décembre. Daily Bulletin of the Observatoire Volcanologique du Piton de la Fournaise, 10 December 2010, OVPF_20101210_1

Di Muro A (2010g) Bulletin Volcanologique du 10 Décembre. Daily Bulletin of the Observatoire Volcanologique du Piton de la Fournaise, 10 December 2010, OVPF_20101210_2

Di Muro A, Staudacher T, Ferrazzini V, Métrich N, Besson P, Garofalo C, Villemant B (2015) Shallow magma storage at Piton de la Fournaise volcano after 2007 summit caldera collapse tracked in Pele's hairs. In: Carey RJ, Cayol V, Poland MP, Weis D (eds.), Hawaiian Volcanoes: From Source to Surface, American Geophysical Union Monograph 208:189 212

Dietterich HR, Cashman KV (2014) Channel networks within lava flows: formation, evolution, and implications for flow behavior. J Geophys Res Earth Surf 119(8):1704 1724. https://doi.org/10.1002/2014JF003103

Dietterich HR, Cashman KV, Rust AC, Lev E (2015) Diverting lava flows in the lab. Nat Geosci 8(7):494 496. https://doi.org/10.1038/ngeo2470

DYNVOLC Database. Observatoire de Physique du Globe de Clermont Ferrand, Aubière, France. https://doi.org/10.25519/DYNVOLC Database

Favalli M, Harris AJL, Fornaciai A, Pareschi MT, Mazzarini F (2010) The distal segment of Etna's 2001 basaltic lava flow. Bull Volcanol 72:119 127. https://doi.org/10.1007/s00445 009 0300 z

Favalli M, Fornaciai A, Nannipieri L, Harris A, Calvari S, Lormand C (2018) UAV based remote sensing surveys of lava flow fields: a case study from Etna's 1974 channel fed lava flows. Bull Volcanol 80:29. https://doi.org/10.1007/s00445 018 1192 6

Garry WB, Zimbelman JR, Gregg TK (2007) Morphology and emplace ment of a long channeled lava flow near Ascraeus Mons Volcano, Mars. J Geophys Res Planets 112(E8). https://doi.org/10.1029/2006JE002803

Glaze LS, Baloga SM, Fagents SA, Wright R (2014) The influence of slope breaks on lava flow surface disruption. J Geophys Res Solid Earth 119(3):1837 1850. https://doi.org/10.1002/2013JB010696

Gurioli L, Di Muro A, Vlastélic I, Moune S, Thivet S, Valer M, Villeneuve N, Boudoire G, Peltier A, Bachèlery P, Ferrazzini V, Métrich N, Benbakkar M, Cluzel N, Constantin C, Devidal JL, Fonquernie C, Hénot JM (2018) Integrating field, textural, and geo chemical monitoring to track eruption triggers and dynamics: a case study from Piton de la Fournaise. Solid Earth 9(2):431 455. https://doi.org/10.5194/se 9 431 2018

Hammer JE, Cashman KV, Voight B (2000) Magmatic processes revealed by textural and compositional trends in Merapi dome lavas. J Volcanol Geotherm Res 100(1):165 192. https://doi.org/10.1016/S0377 0273(00)00136 0

Harris AJL, Rowland SL (2001) FLOWGO: a kinematic thermo rheological model for lava flowing in a channel. Bull Volcanol 63(1):20 44. https://doi.org/10.1007/s004450000120

Harris AJL, Rowland SK (2009). Effusion rate controls on lava flow length and the role of heat loss: a review. In: Thordarson T, Self S, Larsen G, Rowland SK & Hoskuldsson A (eds) Studies. In Volcanology: the legacy of George Walker. IAVCEI, Special Publications 2:33 51

Harris AJL, Murray JB, Aries SE, Davies MA, Flynn LP, Wooster MJ, Wright R, Rothery DA (2000) Effusion rate trends at Etna and Krafla and their implications for eruptive mechanisms. J Volcanol Geotherm Res 102:237 270. https://doi.org/10.1016/S0377 0273(00)00190 6

Harris AJL, Flynn LP, Matias O, Rose WI, Cornejo J (2004) The evolu tion of an active silicic lava flow field: an ETM+ perspective. J Volcanol Geotherm Res 135(1):147 168. https://doi.org/10.1016/j.jvolgeores.2003.12.011

Harris AJL, Dehn J, Calvari S (2007) Lava effusion rate definition and measurement: a review. Bull Volcanol 70:1 22. https://doi.org/10.1007/s00445 007 0120 y

Harris AJ, Rhéty M, Gurioli L, Villeneuve N, Paris R (2015) Simulating the thermorheological evolution of channel contained lava: FLOWGO and its implementation in EXCEL. Geol Soc Spec Publ 426:SP426 9

Harris AJL, Rhéty M, Gurioli L, Villeneuve N, Paris R (2016) Simulating the thermorheological evolution of channel contained lava: FLOWGO and its implementation in EXCEL. Geol Soc Spec Publ 426(1):313 336. https://doi.org/10.1144/SP426.9

Harris AJ, Belousov A, Calvari S, Delgado Granados H, Hort M, Koga K, Mei E, Harijoko A, Pacheco J, Prival J, Solana C, Poroarson P, Thouret J, Van Wyk De Vries B (2017) Translations of volcanolog ical terms: cross cultural standards for teaching, communication, and reporting. Bull Volcanol 79(7):57. https://doi.org/10.1007/s00445 017 1141 9

Heltz RT, Thornber CR (1987) Geothermometry of Kīlauea Iki lavas, Hawaii. Bull Volcanol 49:651 668. https://doi.org/10.1007/BF01080357

Houghton BF, Wilson CJN (1989) A vesicularity index for pyroclastic deposits. Bull Volcanol 51(6):451 462. https://doi.org/10.1007/BF01078811

Huppert H (1982) Flow and instability of a viscous current down a slope. Nature 300:427 429. https://doi.org/10.1038/300427a0

Jeffreys H (1925) The flow of water in an inclined channel of rectangular section. Philos Mag 49:793 807. https://doi.org/10.1080/14786442508634662

Keszthelyi L, Denlinger R (1996) The initial cooling of pāhoehoe flow lobes. Bull Volcanol 58(1):5 18. https://doi.org/10.1007/s004450050121

Kilburn CRJ, Guest JE (1993) 'A'a lavas of Mount Etna, Sicily. In: Active lava. UCL Press, London, pp 73 106

Kilburn CRJ, Lopes RMC (1988) The growth of aa lava fields on Mount Etna, Sicily. J Geophys Res 93:14,759 14,772. https://doi.org/10.1029/JB093iB12p14759

Krauskopf KB (1948) Lava movement at Paricutin volcano, Mexico. Geol Soc Am Bull 59(12):1267 1284. https://doi.org/10.1130/0016 7606(1948)59[1267:LMAPVM]2.0.CO;2

Lev E, James MR (2014) The influence of cross sectional channel geom etry on rheology and flux estimates for active lava flows. BullVolcanol 76:1 15. https://doi.org/10.1007/s00445 014 0829 3

Lipman PW, Banks NG (1987) 'A'ā flow dynamics, Mauna Loa 1984. US Geol Surv Prof Pap 1350:1527 1567

Lister JR (1992) Viscous flows down an inclined plane from point and line sources. J Fluid Mech 242:631 653. https://doi.org/10.1017/S0022112092002520

Llewellin EW, Mader HM, Wilson SDR (2002) The constitutive equation and flow dynamics of bubbly magmas. Geophys Res Lett 29(24):23 1

Mader HM, Llewellin EW, Mueller SP (2013) The rheology of two phase magmas: a review and analysis. J Volcanol Geotherm Res 257:135 158. https://doi.org/10.1016/j.jvolgeores.2013.02.014

Moore HJ (1987) Preliminary estimates of the rheological properties of 1984 Mauna Loa lava. US Geol Surv Prof Pap 1350:1569 1588

Naranjo JA, Sparks RSJ, Stasiuk MV, Moreno H, Ablay GJ (1992) Morphological, structural and textural variations in the 1988 1990 andesite lava of Lonquimay Volcano, Chile. Geol Mag 129(6):657 678. https://doi.org/10.1017/S0016756800008426

Noguchi S, Toramaru A, Nakada S (2008) Relation between microlite textures and discharge rate during the 1991 1995 eruptions at Unzen, Japan. J Volcanol Geotherm Res 175(1 2):141 155. https://doi.org/10.1016/j.jvolgeores.2008.03.025

Parfitt EA, Wilson L, Head III JW (1993) Basaltic magma reservoirs: factors controlling their rupture characteristics and evolution. J Volcanol Geotherm Res 55(1 2):1 14

Peltier A, Bachèlery P, Staudacher T (2009) Magma transport and storage at Piton de La Fournaise (La Réunion) between 1972 and 2007: a review of geophysical and geochemical data. J Volcanol Geotherm Res 184(1):93 108. https://doi.org/10.1016/j.jvolgeores.2008.12.008

Peterson DW, Tilling RI (1980). Transition of basaltic lava from pāhoehoe to aa, Kilauea Volcano, Hawaii: field observations and key factors. J Volcanol Geotherm Res 7(3 4):271 293

Pioli L, Pistolesi M, Rosi M (2014) Transient explosions at open vent volcanoes: the case of Stromboli (Italy). Geology 42(10):863 866. https://doi.org/10.1130/G35844.1

Putirka KD (2005) Igneous thermometers and barometers based on pla gioclase + liquid equilibria: tests of some existing models and new calibrations. Am Mineral 90(2 3):336 346. https://doi.org/10.2138/am.2005.1449

Putirka KD (2008) Thermometers and barometers for volcanic systems. Rev Mineral Geochem 69(1):61 120. https://doi.org/10.2138/rmg.2008.69.3

Putirka K, Johnson M, Kinzler R, Longhi J, Walker D (1996) Thermobarometry of mafic igneous rocks based on clinopyroxene

liquid equilibria, 0 30 kbar. Contrib Mineral Petrol 123(1):92 108. https://doi.org/10.1007/s004100050145

Putirka KD, Perfit M, Ryerson FJ, Jackson MG (2007) Ambient and excess mantle temperatures, olivine thermometry, and active vs. passive upwelling. Chem Geol 241(3):177 206. https://doi.org/10.1016/j.chemgeo.2007.01.014

Rhéty M (2014) Down channel cooling and crystallization of lava during a short lived eruption. B.Sc. thesis, Université Blaise Pascal

Rhéty M, Harris A, Villeneuve N, Gurioli L, Médard E, Chevrel O, Bachélery P (2017) A comparison of cooling limited and volume limited flow systems: examples from channels in the Piton de la Fournaise April 2007 lava flow field. Geochem Geophys Geosyst 18:3270 3291. https://doi.org/10.1002/2017GC006839

Richardson JA (2016). Modeling the construction and evolution of dis tributed volcanic fields on Earth and Mars. Dissertation, University of South Florida

Riker JM, Cashman KV, Kauahikaua JP, Montierth CM (2009) The length of channelized lava flows: insight from the 1859 eruption of Mauna Loa Volcano, Hawai ‘i. J Volcanol Geotherm Res 183(3):139 156. https://doi.org/10.1016/j.jvolgeores.2009.03.002

Robert B, Harris A, Gurioli L, Médard E, Sehlke A, Whittington A (2014) Textural and rheological evolution of basalt flowing down a lava channel. Bull Volcanol 76(6):824. https://doi.org/10.1007/s00445 014 0824 8

Roult G, Peltier A, Staudacher T, Ferrazzini V, Taisne B, Di Muro A, The OVPF Team (2012) A comprehensive classification of the Piton de la Fournaise eruptions (La Réunion Island) spanning the 1986 2010 period Search for eruption precursors from the broad band GEOSCOPE RER station analysis and interpretation in terms of volcanic processes. J Volcanol Geotherm Res 241:78 104. https://doi.org/10.1016/j.jvolgeores.2012.06.012

Ryerson FJ, Weed HC, Piwinskii AJ (1988) Rheology of subliquidus magmas: 1. Picritic compositions. J Geophys Res Solid Earth 93(B4):3421 3436. https://doi.org/10.1029/JB093iB04p03421

Sehlke A, Whittington AG, Robert B, Harris AJL, Gurioli L, Médard E (2014) Pāhoehoe to ‘a‘ā transition of Hawaiian lavas: an experimental study. Bull Volcanol 76:876. https://doi.org/10.1007/s00445 014 0876 9

Shea T, Houghton BF, Gurioli L, Cashman KV, Hammer JE, Hobden BJ (2010) Textural studies of vesicles in volcanic rocks: an integrated methodology. J Volcanol Geotherm Res 190(3):271 289. https://doi.org/10.1016/j.jvolgeores.2009.12.003

Soldati A, Sehlke A, Chigna G, Whittington A (2016) Field and experi mental constraints on the rheology of arc basaltic lavas: the January 2014 eruption of Pacaya (Guatemala). Bull Volcanol 78(6):43. https://doi.org/10.1007/s00445 016 1031 6

Soule SA, Cashman KV, Kauahikaua JP (2004) Examining flow em placement through the surface morphology of three rapidly emplaced, solidified lava flows, Kīlauea Volcano, Hawai'i. Bull Volcanol 66(1):1 14. https://doi.org/10.1007/s00445 003 0291 0

Sparks RSJ, Pinkerton H, Hulme G (1976) Classification and formation of lava levees on Mount Etna, Sicily. Geology 4(5):269 271. https://doi.org/10.1130/0091 7613(1976)4<269:CAFOLL>2.0.CO;2

Tarquini S (2017) A review of mass and energy flow through a lava flow system: insights provided from a non equilibrium perspective. Bull Volcanol 79(8):64. https://doi.org/10.1007/s00445 017 1145 5

Villeneuve N, Bachèlery P (2006). Revue de la typologie des éruptions au Piton de La Fournaise, processus et risques volcaniques associés. Cybergeo: Eur J Geogr 336. https://doi.org/10.4000/cybergeo.2536

Wadge G (1981) The variation of magma discharge during basaltic erup tions. J Volcanol Geotherm Res 11:139 168. https://doi.org/10.1016/0377 0273(81)90020 2

Walker GPL (1972) Compound and simple lava flows and flood basalts. Bull Volcanol 35:579 590. https://doi.org/10.1007/BF02596829

Walker GPL, Huntingdon AT, Sanders AT, Dinsdale JL (1973) Lengths of lava flows. Philos Trans A Math Phyl Eng Sci 274(1238):107 118. https://doi.org/10.1098/rsta.1973.0030

Welsch B, Faure F, Bachèlery P, Famin V (2009) Microcrysts record transient convection at Piton de la Fournaise volcano (La Réunion hotspot). J Petrol 50(12):2287 2305. https://doi.org/10.1093/petrology/egp076